Synthesis and characterization of a nanocrystalline diamond aerogel

Peter J. Pauzauskie[a,1,2], Jonathan C. Crowhurst[a], Marcus A. Worsley[a], Ted A. Laurence[a], A. L. David Kilcoyne[b], Yinmin Wang[a], Trevor M. Willey[a], Kenneth S. Visbeck[a], Sirine C. Fakra[b], William J. Evans[a], Joseph M. Zaug[a], and Joe H. Satcher, Jr.[a]

[a]Physical and Life Sciences Directorate, Lawrence Livermore National Laboratory, Livermore, CA 94551; and [b]Advanced Light Source, Lawrence Berkeley National Laboratory, Berkeley, CA 94720

Aerogel materials have myriad scientific and technological applications due to their large intrinsic surface areas and ultralow densities. However, creating a nanodiamond aerogel matrix has remained an outstanding and intriguing challenge. Here we report the high-pressure, high-temperature synthesis of a diamond aerogel from an amorphous carbon aerogel precursor using a laser-heated diamond anvil cell. Neon is used as a chemically inert, near-hydrostatic pressure medium that prevents collapse of the aerogel under pressure by conformally filling the aerogel's void volume. Electron and X-ray spectromicroscopy confirm the aerogel morphology and composition of the nanodiamond matrix. Time-resolved photoluminescence measurements of recovered material reveal the formation of both nitrogen- and silicon- vacancy point-defects, suggesting a broad range of applications for this nanocrystalline diamond aerogel.

gigapascal | nanomaterials | phase transition | photonics | qubit

Aerogels are a fascinating class of high surface-area continuous solids with a broad range of both commercial and fundamental scientific applications (1–8). Both crystalline and amorphous structures have been synthesized. Amorphous carbon aerogel in particular has received a considerable amount of attention in recent years owing to its low cost, electrical conductivity, mechanical strength, and thermal stability (9). Numerous applications have been explored for this material including water desalination (10), electrochemical supercapacitors (11), as well as both thermal (12) and optical (13) insulation. Impressive advances have been made in the case of polycrystalline aerogels through the oxidative aggregation of chalcogenide quantum dots that preserve spectral signatures of quantum confinement (14). Furthermore, recent high-pressure, high-temperature (HPHT) experiments with mesoporous silica and periodic carbon have been employed to produce mesoporous coesite (15, 16) and diamond (17) structures.

Despite much progress in achieving phase transitions in mesoporous materials, the transition from an amorphous to a crystalline phase in carbon aerogel materials has remained a challenge. The extremely low density and irregular pore structure in aerogel materials make preventing pore collapse a formidable obstacle. Such a nondestructive transition would nevertheless be desirable, because a porous, three-dimensional self-supporting structure consisting of diamonds would have unprecedented optical, thermal, and chemical properties while still maintaining the inherent advantages of aerogel morphology. For instance, diamond aerogel promises a widely tunable optical index of refraction ($\sim 1 < n < 2.4$) for antireflection coatings, biocompatibility, chemical doping, potentially enhanced thermal conduction, as well as electrical field emission applications while still maintaining the low-density, high surface area and self-supporting aerogel morphology. Such a material is particularly intriguing in light of the numerous scientific and technological applications of conventional nanodiamonds, which range from optical quantum bits (18) to cellular biomarkers (19). Here we demonstrate the experimental feasibility of maintaining the morphology of a carbon aerogel through an induced HPHT amorphous-to-crystalline phase transition.

Results and Discussion

In order to affect the transition to diamond we first pressurize the amorphous precursor material sufficiently to enter the diamond stability range of the carbon phase diagram (20) and then heat the sample to overcome kinetic barriers. This is accomplished experimentally using a laser-heated diamond anvil cell (LHDAC) (Fig. 1*A*).

The amorphous precursor aerogel (of density 0.040 g/cm^3, see *SI*) was placed into the diamond cell sample cavity (Fig. 1*A*), which was then filled with supercritical neon at approximately 22,000 psi. We note that while the precursor is self-supporting it is still relatively delicate at least on length scales larger than a few micrometers. Finger pressure, for example, is enough to visibly collapse it. Because our nominal aim was to preserve the aerogel's structure on all length scales larger than the interatomic, it was vital to ensure it was as near as possible hydrostatically supported at the pressures chosen for synthesis. Ideally, the pressure on the inside and outside of the material should be equal and there should be a uniform pressure across the entire sample. Neon is a commonly used pressure transmitting medium in diamond anvil cell experiments and provides a reasonable approximation to a hydrostatic environment at even quite high pressures. At room temperature neon freezes at approximately 4.7 GPa (21), which is well below the pressures chosen here for synthesis; however, it is expected to remain relatively soft. Also, because it was in the supercritical state during the initial high-pressure gas loading of the diamond cell (*SI Text*) it was assumed to completely fill the aerogel without encountering resistance due to for example surface tension. Furthermore, neon's inertness made chemical reactions with the sample extremely unlikely while its transparency facilitates optical microscopy, Raman spectroscopy, and laser heating.

Results presented here were mostly obtained from three separate experiments in which amorphous precursor samples were compressed to approximately 21.0 GPa, 22.5 GPa, and 25.5 GPa. The samples were then laser heated in order to drive the transition to diamond. We chose this pressure range in order to favor the formation of diamond, but we did not attempt to establish a

[1]To whom correspondence should be addressed. E-mail: peterpz@uw.edu.

[2]Present address: Department of Materials Science and Engineering, University of Washington, Seattle, WA, 98195.

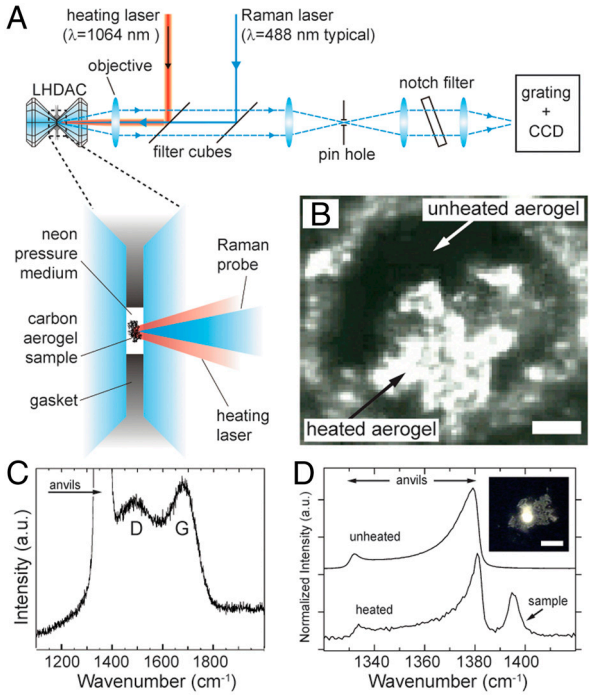

Fig. 1. Synthesis of diamond aerogel from amorphous carbon aerogel precursor under high pressure and temperature. (*A*) Schematic of optical system used to heat the sample contained in the diamond anvil cell and to perform in situ Raman spectroscopy (see *SI Text* for details). The carbon aerogel precursor is laser heated to likely more than 1,600 K at several pressures between approximately 21 to 26 GPa in order to drive the transition to diamond. Dashed lines show path followed by collected light. (*B*) Optical transmission micrograph of synthesized diamond aerogel above 20 GPa following laser heating. Translucent regions were laser heated while dark regions were not heated as a control. Surrounding material is the rhenium metal gasket. Scale bar: 20 μm. (*C*) Raman spectrum of amorphous precursor at approximately 22.5 GPa showing both D and G modes consistent with prior reports of amorphous carbon. The intense peak between 1,300 cm^{-1} and 1,400 cm^{-1} is due to the diamond anvil or anvils. (*D*) Comparison of the Raman spectrum in *C* with that obtained after heating (note difference in x-axis scale from *C*). The additional peak is due to newly formed diamond. The peak is resolvable from that of the anvils because of the different stress states and the spatial selection of the instrument. The difference in signal-to-noise is partly attributed to intense fluorescence from the diamond aerogel (Fig. S1). Inset: Optical micrograph of fluorescence from diamond aerogel. Scale bar: 50 μm.

minimum synthesis pressure, or more generally the required minimum combined conditions of pressure and temperature. Furthermore, precise determination of temperature was complicated by a number of factors including sample motion during heating in the melted neon. In a single separate experiment in argon in which sample motion was reduced, and on the basis of measured thermal emission data, we concluded that synthesis temperature likely exceeds 1,580 K ± 40 K (see *SI Text* for important details).

Raman spectroscopy was used to characterize the state of the sample and monitor the transition from amorphous to crystalline diamond. The amorphous carbon aerogel sample appears completely opaque before heating, owing to its strong broadband absorbance (13). The material becomes highly transparent following laser heating and was observed to transmit a large amount of incident light in comparison with the amorphous precursor (Fig. 1*B*). Raman spectra were acquired from the carbon aerogel after pressurizing and before heating (Fig. 1*C* and Fig. S1) and were found to be similar to prior reports on amorphous carbon aside from pressure-induced shifts. This observation rules out the possibility of a superhard graphite phase helping to prevent pore collapse, which has been hypothesized for mesoporous carbon (17) given that the spectrum still appears amorphous after pressurizing. Spectra obtained following laser heating (Fig. 1*D* and Fig. S1) revealed a new sharp peak between approximately 1,390 cm^{-1} and 1,404 cm^{-1} (depending on the pressure) and the pressure dependence of this mode was consistent with cubic crystalline diamond (Fig. S2). Furthermore, intense fluorescence was visible during Raman measurements from the laser-heated material, which was retained at ambient conditions (Fig. 1*D Inset*), suggesting the potential formation of luminescent point defects in the newly formed diamond phase. Aside from the fact that diamond is favored thermodynamically, we also note that recent theoretical and experimental reports have demonstrated hydrogen-catalyzed synthesis of diamond nanocrystals (22). Carbon–hydrogen bonds are observable in the infrared absorption spectra of the amorphous carbon starting material (Fig. S3) and may catalytically enhance kinetics of the phase transition.

Transmission electron microscopy (TEM) of recovered material (Fig. 2 *A* and *B*) revealed that the highly porous aerogel morphology of the precursor appears well preserved in the recovered material, while electron diffraction (Fig. 2 *C* and *D*) confirms the conversion from amorphous carbon to cubic diamond. The presence of the diamond phase is confirmed further through high resolution TEM images (Fig. 2 *E* and *F*). The amorphous starting material consists of interconnected graphitic domains with sizes of approximately 10 nm, in agreement with previous reports for

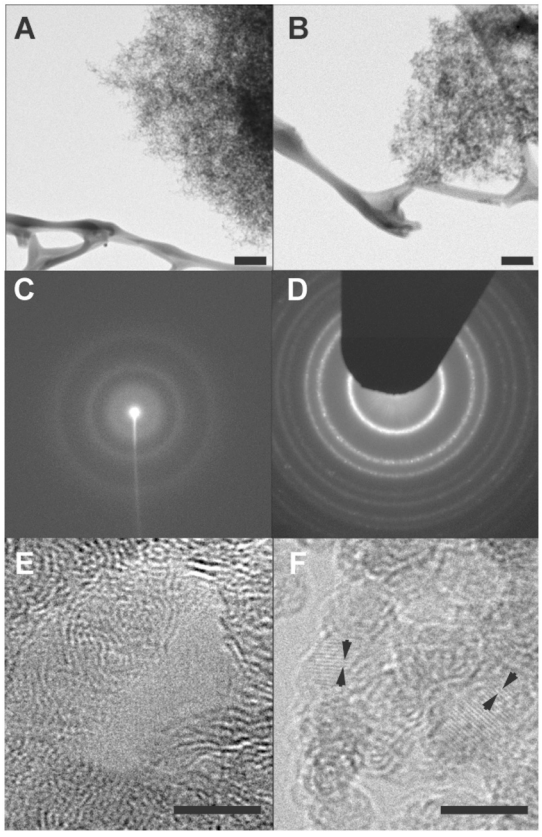

Fig. 2. Transmission electron micrographs of amorphous carbon precursor and recovered diamond aerogel. (*A* and *B*) Bright-field transmission electron micrographs of amorphous aerogel (*A*) and recovered aerogel (*B*). Samples are supported on lacy carbon. Scale bars: 200 nm. (*C* and *D*) Corresponding electron diffraction from precursor and recovered material, respectively. (In *D* the fundamental beam is blocked.) (*E* and *F*) High resolution images of carbon and diamond aerogel microstructure. Nanocrystalline lattice fringes visible in *F* (arrowheads) correspond to the (111) plane of cubic diamond with a lattice spacing of 2.06 Å. Scale bars: 5 nm.

carbon aerogel (9). In contrast, the recovered diamond aerogel material consists of nanocrystalline grains connected through what appears to be thin surface coatings of graphitic carbon. Individual grains range in size from 2.5 to 100 nm and at high resolution show sharp lattice fringes with a d-spacing of approximately 2.06 Å corresponding to the (111) plane of cubic diamond (Fig. 2*F*). We assume this size distribution is due to the extent of heating, which depends on how well incident laser light is absorbed by different regions of the sample. Also, melting of the neon medium may facilitate agglomeration and crystal growth. High resolution SEM analysis (Fig. S4) is consistent with TEM observations. The measured Raman spectra after heating are likely dominated by the presence of the larger diamond grains because the corresponding frequencies and line shape are consistent with diamonds of grain size >10 nm (see ref. 23). Electron energy loss spectroscopy spectra (Fig. S5), obtained from this material with 1.8-eV resolution, show the characteristic second gap of diamond at 302.5 eV as well as a small sp^2 graphitic π^* absorption shoulder at 285.5 eV. The sp^2 absorption is consistent with the diamond nanocrystals having thin surface coatings of graphitic carbon; however, this energy resolution is insufficient to completely resolve pre-edge features.

Comparison of the recovered aerogel with other types of nanodiamond aids in the characterization of the aerogel's composition. Fig. 3 and Fig. S6 show high energy resolution (approximately 100 meV) C 1s near-edge X-ray absorption fine structure (NEXAFS) data measured on the aerogel materials using scanning transmission X-ray microscopy (STXM) as well as total electron yield (TEY) mode on bulk diamond and detonation nanodiamonds of 4 nm diameter. While the precursor aerogel exhibits predominantly sp^2 carbon, the diamond aerogel spectrum distinctly resembles the predominantly sp^3 detonation nanodiamond spectrum (24). This includes the characteristic second gap in the diamond band structure at 302.5 eV, which has been shown to become less pronounced with decreasing crystallite size in nanodiamond materials (25). The C 1s $\rightarrow \pi^*$ transitions at 285 and 287 eV in the spectra of the aerogel and detonation nanocrystals match remarkably well in both energy position and intensity. They are characteristic of sp^2 carbon and have been attributed to a fullerene-like surface reconstruction on the diamond nanoparticles (24). This agrees with TEM results (Fig. 2*F*), which show thin surface coatings consistent with graphitic carbon. The fundamental similarities between the spectra for STXM spectra of diamond aerogel and TEY spectra of detonation nanodiamonds give a clear indication from sampling many grains ($>10^3$) that the diamond aerogel consists of nanodiamond crystallites of similar composition, morphology, and surface reconstruction as clean detonation nanodiamonds.

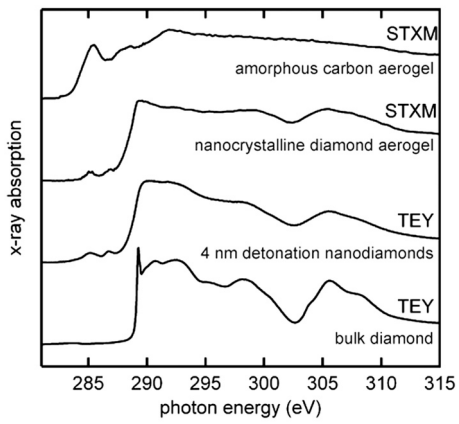

Fig. 3. C 1s near-edge X-ray absorption fine structure (NEXAFS) spectromicroscopy. Comparison of scanning transmission X-ray absorption microscopy (STXM) spectra of amorphous carbon precursor and diamond aerogel with total electron yield (TEY) spectra of both 4 nm detonation nanodiamond and bulk single crystal diamond. Amorphous carbon aerogel is predominantly graphitic as indicated by the strong $\pi*$ absorption at 285.5 eV. In contrast, the recovered diamond aerogel material shows the characteristic second gap structure in carbon's conduction-band electronic density-of-states near 302.5 eV.

Another dramatic new property of the recovered diamond aerogel in comparison with the amorphous starting material is the presence of bright and photostable luminescence. Fig. 4*A* shows a bright-field TEM image from a segment of recovered diamond aerogel material that contains several different diamond grain sizes, from 2.5 to 100 nm. Two pronounced features are observed in the photoluminescence spectrum (Fig. 4*B*): a broad feature starting at approximately 639 nm and a sharper feature at approximately 739 nm. These wavelengths are comparable to those of the well known negatively charged nitrogen-vacancy $(N-V)^-$ (26) and neutral silicon di-vacancy (V-Si-V) (27) centers, respectively. These features were not observed in all recovered material and likely result from the unintended presence of both N and Si in the precursor aerogel. Confocal fluorescence images were collected from recovered diamond aerogel (Fig. 4*C*) in conjunction with time correlated single photon counting (TCSPC) of both small and large grains (Fig. 4*D*), which were spectrally filtered around the nitrogen-vacancy peak. The TCSPC data indicate that the emission lifetime from the aerogel in the 639-nm spectral region has an approximately 10-ns component (Fig. 4*D*, blue) characteristic of the negatively charged $(N-V)^-$ center (28), which is a prime candidate for future quantum information processing (29, 30). Furthermore, TCSPC data for the 739-nm spectral region (Fig. S7 and S8) shows a lifetime of approximately 1 ns, consistent with the (V-Si-V) center, which has been proposed as a biocompatible near-infrared fluorophore (31).

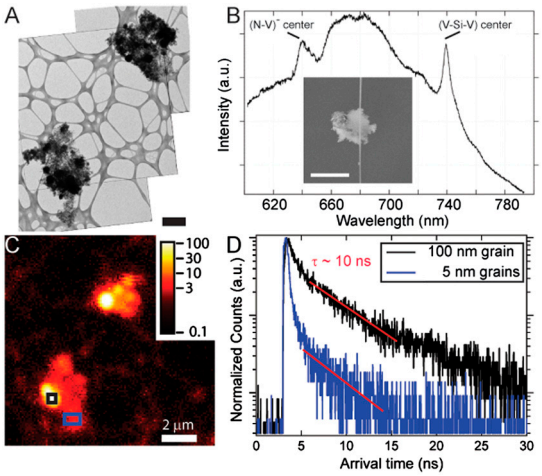

Fig. 4. Time-resolved photoluminescence spectroscopy. (*A*) Bright-field TEM micrograph showing recovered diamond aerogel material showing a range of grain sizes. Scale bar: 1 μm. (*B*) Visible photoluminescence spectrum of recovered diamond aerogel material excited at $\lambda = 488$ nm. Features at 639 nm and 739 nm are likely due to zero-phonon loss nitrogen vacancy $(N-V)^-$ and silicon di-vacancy (V-Si-V) centers, respectively. Inset: SEM micrograph of diamond aerogel supported on a silicon nanowire. Scale bar: 5 μm. (*C*) Confocal fluorescence image of recovered diamond aerogel supported on a lacy carbon grid. The region indicated by the black and blue rectangles indicate a large 100-nm diamond grain and fine diamond aerogel material, respectively. Scale indicates count rate in kHz. (*D*) Fluorescence lifetime data from time correlated single photon counting for emission from a large diamond grain of approximately 100 nm (black) and the diamond aerogel material with approximately 5 nm grains (blue). Both the large grain and the 5-nm grain diamond aerogel emission have a lifetime component of approximately 10 ns (from slope of red best fit lines), consistent with the presence of $(N-V)^-$ centers.

Conclusion

We present a general experimental approach for preserving the mass-fractal microstructure of an amorphous carbon aerogel through a phase change to a polycrystalline diamond aerogel. Novel scientific applications of diamond aerogel are expected as a consequence of the unique physical properties of diamond compared with amorphous carbon, as well as from the chemical flexibility of the amorphous aerogel's aqueous synthesis. This method is likely to be general and may be extended to produce previously unachieved crystalline aerogel phases (starting from, for example, amorphous SiO_2) with potential relevance as materials with enhanced energy storage and production capabilities (32). No attempt was made here to determine the minimum combined conditions of pressure and temperature required for synthesis, which might in fact be substantially less extreme and applicable on a larger scale, assuming a suitable candidate material to support the aerogel under pressure. Future work will be directed at establishing minimal thermodynamic conditions for the phase transition as well as tailoring the amorphous precursor to produce nanostructured diamond materials with novel compositions and unrealized three-dimensional morphologies (33).

Materials and Methods

Pressures were obtained in situ in the diamond cell using the technique based on ruby fluorescence. Carbon aerogel sample material was loaded into the diamond cell cavity using hand held needles in air. Neon (Airgas-Specialty Gases, UHP) was loaded into the cavity under high pressure (approximately 22,000 psi). Temperatures were not measured in the experiments in a neon medium. In an argon medium a lower limit on the transition temperature was obtained from measured thermal emission data. *SI Text* contains further details for aerogel synthesis, diamond anvil cell loading, Raman spectroscopy, laser heating, temperature estimation, TCSPC, STXM, and TEY techniques.

ACKNOWLEDGMENTS. The authors thank A. Goncharov for assistance in determining LHDAC temperatures from thermal emission data, as well as L. Hrubesh, L. Fried, D. Awschalom, M. Armstrong, C. Grant, T. Baumann, P. Weber, J. Bradley, I. Hutcheon, W. Goldstein, and G. Fox for valuable comments, and I. Hutcheon for access to SEM facilities. Use of the Advanced Light Source is supported by the US Department of Energy, Office of Science, Office of Basic Energy Sciences, under Contract DE-AC02-05CH11231. This work performed under the auspices of the US Department of Energy by the Lawrence Livermore National Laboratory (LLNL) under Contract DE-AC52-07NA27344. P.J.P. gratefully acknowledges funding from an E.O. Lawrence Fellowship at the LLNL.

1. Brinker CJ, Scherer GW (1990) *Sol-Gel Science: The Physics and Chemistry of Sol-Gel Processing* (Academic, San Diego).
2. Hrubesh LW (1998) Aerogel applications. *J Non-Cryst Solids* 225:335–342.
3. Baumbardner JE, Lee Y, Osheroff DD, Hrubesh LW, Poco JW (2004) Interfacial pinning in the superfluid He-3 A-B transition in aerogel. *Phys Rev Lett* 93:055301–4.
4. Obrey KAD (2009) Manufacturing complex silica aerogel target components. *Fusion Sci Technol* 55:490–498.
5. Fan SK, et al. (2001) MEMS with thin-film aerogel. *Proc IEEE Micr Elect* 2001:122–125.
6. Cremaldi L, Sanders DA, Sonnek P, Summers DJ, Reidy J (2009) A Cherenkov radiation detector with high density aerogels. *IEEE T Nucl Sci* 56:1475–1478.
7. Schaefer DW (1989) Polymers, fractals, and ceramic materials. *Science* 243:1023–1027.
8. McKeegan KD, et al. (2006) Isotopic compositions of cometary matter returned by Stardust. *Science* 314:1724–1728.
9. Pekala RW, Alviso CT, Kong FM, Hulsey SS (1992) Aerogels derived from multifunctional organic monomers. *J Non-Cryst Solids* 145:90–98.
10. Farmer JC, Fix DV, Mack GV, Pekala RW, Poco JF (1996) Capacitive deionization of NaCl and $NaNO_3$ solutions with carbon aerogel electrodes. *J Electrochem Soc* 143:159–169.
11. Lukens WW, Stucky GD (1989) Synthesis of mesoporous carbon foams templated by organic colloids. *Chem Mater* 14:1665–1670.
12. Hrubesh LW, Pekala RW (1994) Thermal-properties of organic and inorganic aerogels. *J Mater Res* 9:731–738.
13. Merzbacher CI, Meier SR, Pierce JR, Korwin ML (2001) Carbon aerogels as broadband non-reflective materials. *J Non-Cryst Solids* 285:210–215.
14. Mohanan JL, Arachchige IU, Brock SL (2005) Porous semiconductor chalcogenide aerogels. *Science* 307:397–400.
15. Mohanty P, Fei Y, Landskron K (2009) Synthesis of periodic mesoporous coesite. *J Am Chem Soc* 131:9638–9639.
16. Mohanty P, et al. (2010) Direct formation of mesoporous coesite single crystals from periodic mesoporous silica at extreme pressure. *Angew Chem Intl Edit* 49:4301–4305.
17. Zhang L, et al. (2010) Catalyst-free synthesis of transparent, mesoporous diamond monoliths from periodic mesoporous carbon CMK-8. *Proc Natl Acad Sci USA* 107:13593–13596.
18. Weber JR, et al. (2010) Quantum computing with defects. *Proc Natl Acad Sci USA* 107:8513–8518.
19. Fu CC, et al. (2007) Characterization and application of single fluorescent nanodiamonds as cellular biomarkers. *Proc Natl Acad Sci USA* 104:727–732.
20. Bundy FP, et al. (2006) The pressure-temperature phase and transformation diagram for carbon;updated through 1994. *Carbon* 34:141–153.
21. Vos WL, Schouten JA, Young DA, Ross M (1991) The melting curve of neon at high-pressure. *J Chem Phys* 94:3835–3838.
22. Muniz AR, Singh T, Aydil ES, Maroudas D (2009) Analysis of diamond nanocrystal formation from multiwalled carbon nanotubes. *Phys Rev B* 80:144105–12.
23. Osswald S, Mochalin VN, Havel M, Yushin G, Gogotsi Y (2009) Phonon confinement effects in the Raman spectrum of nanodiamond. *Phys Rev B* 80:075419–9.
24. Raty JY, Galli G, Bostedt C, van Buuren TW, Terminello LJ (2005) Quantum confinement and fullerenelike surface reconstructions in nanodiamonds. *Phys Rev Lett* 90:037401–4.
25. Coffman FL, et al. (2006) Near-edge X-ray absorption of carbon materials for determining bond hybridization in mixed sp^2/sp^3 bonded materials. *Appl Phys Lett* 69:568–570.
26. Childress L, et al. (2006) Coherent dynamics of coupled electron and nuclear spin qubits in diamond. *Science* 314:281–285.
27. Goss JP, Jones R, Breuer SJ, Briddon PR, Oberg S (1996) The twelve-line 1.682 eV luminescence center in diamond and the vacancy-silicon complex. *Phys Rev Lett* 77:3041–3044.
28. Jelezko F, Wrachtrup J (2006) Single defect centres in diamond: A review. *Phys Status Solidi A* 203:3207–3225.
29. Hanson R, Dobrovitski VV, Feiguin AE, Gywat O, Awschalom DD (2008) Coherent dynamics of a single spin interacting with an adjustable spin bath. *Science* 320:352–355.
30. Jiang L, et al. (2009) Repetitive readout of a single electronic spin via quantum logic with nuclear spin ancillae. *Science* 326:267–272.
31. Vlasov I, et al. (2009) Nanodiamond photoemitters based on strong narrow-band luminescence from silicon-vacancy defects. *Adv Mater* 21:808–812.
32. Wittstock A, Zielasek V, Biener J, Friend CM, Baumer M (2010) Nanoporous gold catalysts for selective gas-phase oxidative coupling of methanol at low temperature. *Science* 327:319–322.
33. Zakhidov AA, et al. (1998) Carbon structures with three-dimensional periodicity at optical wavelengths. *Science* 282:897–901.